Strongly bound citrate stabilizes the apatite nanocrystals in bone

Y.-Y. Hu, A. Rawal, and K. Schmidt-Rohr[1]

Ames Laboratory and Department of Chemistry, Iowa State University, Ames, IA 50011

Edited by David A. Tirrell, California Institute of Technology, Pasadena, CA, and approved October 12, 2010 (received for review June 27, 2010)

Nanocrystals of apatitic calcium phosphate impart the organic-inorganic nanocomposite in bone with favorable mechanical properties. So far, the factors preventing crystal growth beyond the favorable thickness of *ca.* 3 nm have not been identified. Here we show that the apatite surfaces are studded with strongly bound citrate molecules, whose signals have been identified unambiguously by multinuclear magnetic resonance (NMR) analysis. NMR reveals that bound citrate accounts for 5.5 wt% of the organic matter in bone and covers apatite at a density of about 1 molecule per $(2\ \mathrm{nm})^2$, with its three carboxylate groups at distances of 0.3 to 0.45 nm from the apatite surface. Bound citrate is highly conserved, being found in fish, avian, and mammalian bone, which indicates its critical role in interfering with crystal thickening and stabilizing the apatite nanocrystals in bone.

nanocrystal stabilization | nanocomposite | organic-inorganic interface | bone composition | solid-state NMR

The load-bearing material in bone is a fascinating organic-inorganic nanocomposite whose stiffness is provided by thin nanocrystals of carbonated apatite, a calcium phosphate, imbedded in an organic matrix consisting mostly of collagen, a fibrous protein (1–5). The small (*ca.* 3-nm) thickness of the apatite nanocrystals is favorable for mechanical properties, likely preventing crack propagation (6). While the size and shape of the nanocrystals have been studied extensively (4, 5), the mechanism stabilizing them at a thickness corresponding to only about four unit cells has not been elucidated. A better understanding of the factors controlling the nanocrystals in bone is desirable for prevention and treatment of bone diseases such as osteoporosis, which causes millions of fractures each year (7), and for more efficient synthesis of biomimetic nanocomposites (8, 9). In vitro experiments have shown that carboxylate-rich proteins such as osteocalcin and osteopontin (7) can affect hydroxyapatite crystal formation and growth (10, 11). These observations might suggest that such proteins limit nanocrystal thickening (12); however, these proteins are not sufficiently abundant in vivo to bind to all the nanocrystal surfaces at high enough area concentration; possibly, they control the length of the nanocrystals (7).

Here we show instead that the surfaces of the apatite crystals in bone are studded with strongly bound citrate molecules, at a density of *ca.* $1/(2\ \mathrm{nm})^2$, using advanced solid-state nuclear magnetic resonance (NMR) as a unique tool for probing buried interfaces. Citrate is quite abundant in bone (*ca.* 1 wt%, or 5 wt% of the organic components) (13, 14). Before 1975, citrate in bone was studied by simple wet-chemical methods and thought to regulate bone demineralization (14). However, citrate is no longer even mentioned in most of the prominent literature on the bone nanocomposite published during the last thirty years (1–5, 15–18). We now highlight the importance of citrate in bone by demonstrating that it is not a dissolved calcium-solubilizing agent but a strongly bound, integral part of the nanocomposite. Structurally, citrate stands out among biomolecules in that it contains an oxygen-bonded quaternary (nonprotonated) alkyl carbon, which we have identified by NMR spectral editing. We show that citrate signals dominate the NMR spectra of carbons near the interface with apatite and estimate distances from the apatite surface. Further, we determine the area concentration of apatite-bound citrate and confirm it by quantitative analysis of spin exchange between ^{13}C-labeled citrate adsorbed to purified bone apatite. Thus, a quite comprehensive picture emerges of citrate binding strongly to apatite and inhibiting an increase in apatite nanocrystal thickness.

Results and Discussion

Fig. 1 *A–C* shows the ^{13}C NMR spectra of fish, avian, and bovine bone. Similar to previously published data (17–19), the spectra are dominated by signals of collagen, the fibrous protein rich in glycine (33%), proline, hydroxyproline, and alanine (each 11%) that forms the matrix of the bone nanocomposite. The spectrum of ^{13}C near ^{31}P in bovine bone, obtained by ^{13}C$\{^{31}$P$\}$ rotational echo double resonance (REDOR) NMR (17, 20, 21), i.e., with ^{13}C observation and ^{31}P recoupling pulses, is shown in Fig. 1*D*. Strong signals are observed at 182, 169, 76, and 49 ppm; those at 182 and 76 ppm, as well as the inorganic carbonate signal at 169 ppm, had been detected before (17, 18), but the strong signal intensity near 49 ppm had not been recognized. We assign the peaks at 182, 76, and 49 ppm to citrate (see structure at top of Fig. 1) bound to the apatite surface, because the strong citrate peaks of bone partially exchanged with uniformly ^{13}C-labeled citrate (Fig. 1*E*) and the signal positions of calcium citrate (Fig. 1*F*) provide an excellent match. Citrate contains an oxygen-bonded quaternary (nonprotonated) alkyl carbon, which is quite rare among biomolecules; the slow H—C dipolar dephasing of the 76-ppm signal in both citrate and bone (Fig. 1 *G* and *H*) is a telltale sign of this nonprotonated carbon and thus of citrate. The weak C—H dipolar coupling cannot be attributed to mobility effects, because the ^{1}H wideline spectrum (22) associated with the 76-ppm carbon shows no motional narrowing (Fig. 2). We agree with ref. 17 that the 76- and 182-ppm signals are not from collagen, but the subsequent assignment to sugar residues (18, 19) is not tenable for the majority of this signal, because the C—OH carbons in sugars are protonated, not quaternary. The dominant contribution of the nonprotonated carbon of citrate at 76 ppm and the weak signal of anomeric (O—C—O) carbons near 100 ppm, which is a band characteristic of sugar rings (23), indicates that the polysaccharide concentration is only about 1/4 of that of citrate. The intensity of the 76-ppm quaternary citrate carbon peak (0.75% of the total spectrum) corresponds to a 4.5% signal fraction of all six citrate carbons and *ca.* 5.5 wt% of citrate in the organic component of bone, consistent with wet-chemical analyses in the literature (13, 14).

In order to provide a more detailed picture of the bound citrate, we have determined the distances of various citrate carbons from the apatite surface by analysis of the 76- and 182-ppm signals in bone and in bone exchanged with uniformly ^{13}C-labeled

Author contributions: K.S.-R. designed research; Y.-Y.H., A.R., and K.S.-R. performed research; Y.-Y.H., A.R., and K.S.-R. analyzed data; and K.S.-R. and Y.-Y.H. wrote the paper.

The authors declare no conflict of interest.

This article is a PNAS Direct Submission.

See Commentary on page 22369.

[1]To whom correspondence should be addressed. E-mail: srohr@iastate.edu.

This article contains supporting information online at www.pnas.org/lookup/suppl/doi:10.1073/pnas.1009219107/-/DCSupplemental.

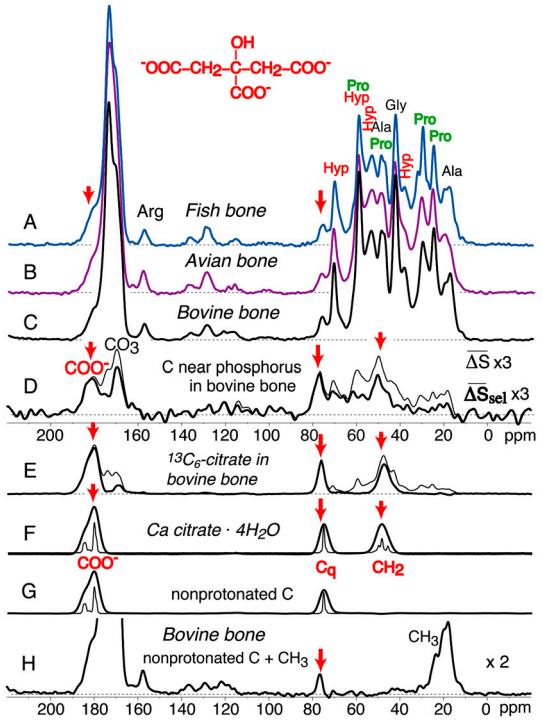

Fig. 1. ^{13}C NMR spectra of bone, of organic residues at the interface with apatite, and of ^{13}C-labeled citrate in bone. (*A*) Fish bone; (*B*) avian bone; and (*C*) bovine bone. (*D*) Spectra of ^{13}C near ^{31}P in bovine bone. Thin line: $^{13}C\{^{31}P\}$ REDOR difference (ΔS) spectrum (total measuring time: 19 d). Thick line: Same data but with the spectrum S scaled up by 1.1 to match the 43-ppm peak of Gly in S_0 and thus remove signal of abundant interior collagen residues. (*E*) Thin line: Spectrum of bovine bone with uniformly ^{13}C-labeled bound citrate, introduced after (partial) removal of native citrate by treatment with hot dilute acid. Thick line: Same data after subtraction of the collagen background, isolating the signals of bound citrate. (*F*) Spectrum of calcium citrate, with minimal line broadening (thin line) and broadened (thick line) to match that in (*D*) and (*E*). (*G*) Same as (*F*) after 40 μs dipolar dephasing, which selects signals of carbons with weak C—H dipolar couplings, i.e., nonprotonated C and mobile CH_n. (*H*) Spectrum of bovine bone after 40 μs dipolar dephasing. Citrate signals are highlighted by red arrows.

citrate, using $^{13}C\{^{31}P\}$ REDOR NMR (filled symbols in Fig. 3 *A* and *B*). A smaller distance gives rise to stronger ^{13}C-^{31}P dipolar couplings and a faster REDOR signal decay. The almost complete

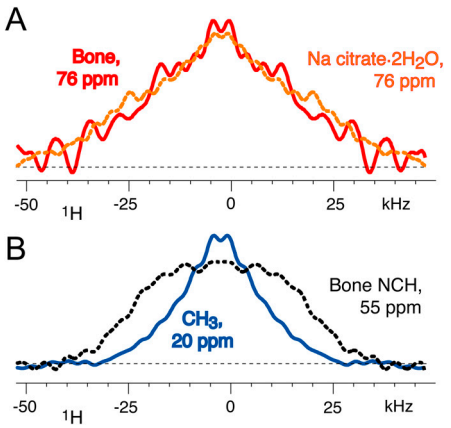

Fig. 2. The 76-ppm ^{13}C NMR signal in bone is from an immobile (nonprotonated) C—OH group. (*A*) Wideline ^{1}H spectra associated with 76-ppm ^{13}C signals in bone (solid red line) and sodium citrate dihydrate (dashed orange line), from ^{1}H-^{13}C wideline-separation NMR. Both show no significant motional narrowing. (*B*) Corresponding ^{1}H spectra of NCH (protein backbone, dashed line) and CH_3 groups. Only the latter, which undergo rotational jumps, exhibit motional narrowing.

long-time dephasing in $^{13}C\{^{31}P\}$ REDOR NMR (Fig. 3*A*) proves that most water-insoluble citrate is close to ^{31}P, i.e., bound to apatite rather than precipitated as sodium or calcium citrate. Multispin analysis of these REDOR data yields a distance of about 0.35 nm between the top ^{31}P layer and citrate carboxylates (for details see *SI Text*). For citrate with ^{13}C-labeled terminal COO^- groups, peaks at 178 and 180 ppm can be deconvoluted. The dephasing of the two peaks is somewhat different, see Fig. 3*A*, corresponding to 0.33 and 0.45 ($\pm$0.05) nm from the top ^{31}P layer, respectively. Strongly asymmetric binding of only one terminal carboxylate to the apatite surface, similar as in simulations of citric acid on hydroxyapatite (24), would result in distances of 0.3 and 0.7 nm; most citrate molecules do not "stand up" like this on bone apatite. Fig. 3*B* shows the REDOR dephasing of other carbons in citrate. On average, the carboxylate carbons are slightly closer to the interface than methylene and quaternary C, consistent with carboxylate binding to calcium of apatite. All citrate carbons are found at about 0.4 nm from the top phosphorus layer, which means that the long axes of the citrate molecules are tilted only slightly relative to the apatite surface. The $^{13}C\{^{31}P\}$ REDOR data also exclude that phosphocitrate, which has been proposed as a major form of citrate in bone (14), is significantly present; the corresponding simulated curve (dashed) for a two-bond ^{13}C-^{31}P distance shows a much faster decay than is observed experimentally.

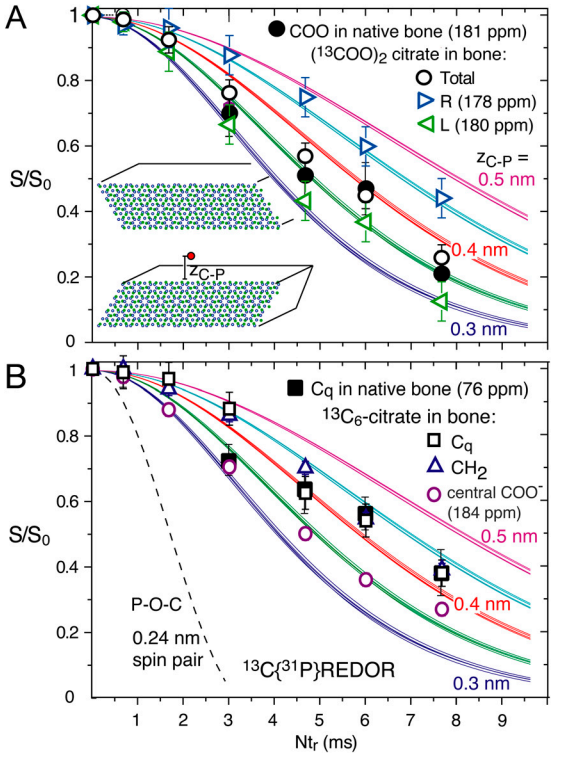

Fig. 3. Determination of distances of citrate carbons from bone apatite, measured by $^{13}C\{^{31}P\}$ REDOR NMR. The measured dephasing S/S_0 is plotted along with simulated curves for distances $z_{C\text{-}P}$ of 0.3, 0.35, 0.4, 0.45, and 0.5 nm of ^{13}C from the first ^{31}P layer at the interface (see inset schematic and Fig. S1). (*A*) Filled black circles: carboxylate resonance at 181 ppm in native bovine bone; open circles: sum of terminal $^{13}COO^-$ groups in ^{13}C-labeled citrate absorbed into bovine bone. Triangles pointing right and left: Dephasing of 178- and 180-ppm ^{13}C citrate signals, respectively. (*B*) Data for the quaternary C-OH of citrate in bone (filled black squares), as well as quaternary C—OH (Cq, open squares), CH_2 (open blue triangles) and the central COO^- (open purple circles) in ^{13}C-labeled citrates absorbed into bovine bone. Error margins were determined from the signal-to-noise ratios in the REDOR spectra. The dashed curve is for a ^{31}C-^{31}P spin pair (two-bond distance of 0.24 nm) as in phosphocitrate.

The citrate area concentration on bone apatite can be calculated from the 3-nm thickness of the crystallites, the composite density of 2.2 g/cm^3, 50 vol% apatite, and 1 wt% citrate (see *SI Text*). The resulting value of about 1 molecule per (2 nm)^2 agrees with that found for citrate on purified bone mineral (deproteinized bovine bone, NuOss™) from the citrate concentration determined by ^{13}C NMR (0.8 mg citrate per 190 mg of bone mineral) and the specific surface area of 60 m^2/g. Given that a citrate molecule has a geometrical area of *ca.* 0.65 nm^2 (25), citrate covers about 1/6 of the available apatite surface area in bone.

In order to investigate the distribution of citrate in more detail, we have probed the local citrate density in terms of ^{13}C-^{13}C dipolar couplings of ^{13}C-labeled terminal COO$^-$ groups in citrate bound to the purified NuOss™ bone mineral, using ^{13}C centerband-only detection of exchange (CODEX) NMR with dipolar ^{13}C spin exchange (26). In short, CODEX NMR yields the fraction of ^{13}C spins that, during a waiting period t_m, have not changed their frequency due to dipolar spin exchange with other ^{13}C nuclear magnets (26). If the doubly ^{13}C-labeled citrate molecules were isolated from their neighbors, the CODEX data would level off at a long-time value of 1/2 (26). The experimental data in Fig. 4 drop below 1/2, proving contacts between different citrate molecules on a 1.5-nm scale. The fast initial decay is due to the ^{13}C spins separated by 0.5 nm within each molecule, while the slope at longer times reflects mostly the distance to the nearest-neighbor molecule. Simulations (described in the *SI Text*) give good fits for area densities near the value of 1/(2 nm)^2 calculated above, with moderate positional ordering of citrate molecules. This result shows that the molecules cover most apatite surfaces with the average area density.

Proof of citrate immobilization can be obtained from the NMR data. The CODEX signal decay would be much more pronounced than observed in Fig. 4 if large-amplitude motions of the carboxylate groups occurred on the 10 s time scale (26). Large-amplitude motions on the 10-μs (or faster) time scale are excluded by the absence of motional narrowing in ^{1}H-^{13}C wide-line separation NMR, see Fig. 2, confirming strong binding of citrate to bone apatite. Thus, citrate cannot be part of a surface layer of hydrated mobile ions proposed by Rey et al. (3).

Based on these structural data, we propose the model of citrate bound to apatite presented in Fig. 5, with a realistic citrate density and orientation. The CH_2 groups of citrate facing the exterior may give the surface a locally less hydrophilic character, making it

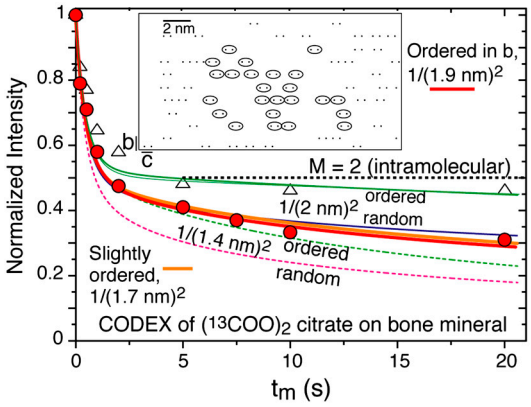

Fig. 4. Distances between apatite-bound citrate molecules, probed by CODEX ^{13}C NMR with ^{13}C spin exchange during the time t_m. Data points (red circles) for citrate with terminal ^{13}COO groups on purified bone mineral are compared with fit curves for seven different citrate distributions (Fig. S2). Data points for 2.5 times less citrate, with little intermolecular spin exchange, are shown for reference as open triangles. Inset: One of the best-fit distributions of ^{13}C spins (black dots), with some citrate molecules identified by ellipses.

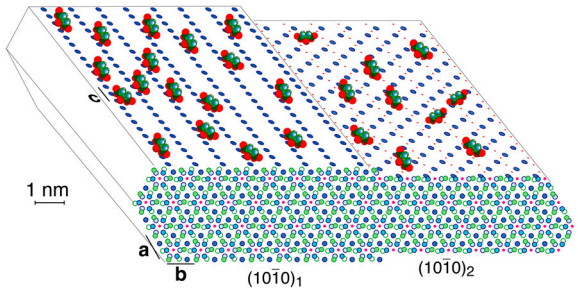

Fig. 5. Schematic of apatite-bound citrate (with oxygen of the carboxylates in red) interacting with Ca^{2+} on two surfaces of high morphological importance of an idealized bone apatite nanocrystal, at a realistic citrate surface density of *ca.* 1/(2 nm)^2. Calcium ions are blue filled circles on top and front surfaces, P is green (omitted on the top surfaces), OH^- ions are pink dots, while phosphate oxygen is omitted for clarity. The hexagonal crystal structure projected along the c-axis (with greater depth of atoms indicated by lighter shading) shown in front reveals various layers of phosphate and calcium ions.

more compatible with the nonpolar proline and alanine residues of the collagen matrix. Apatite is represented as ideal hydroxyapatite, Ca_{10} $(PO_4)_6$ $(OH)_2$ (hexagonal unit cell with $a = b =$ 0.944 nm, $c = 0.688$ nm). Calcium ions in two planes of highest morphological importance (27) are shown on the top left and right. In the $(10\bar{1}0)_1$ plane, Ca^{2+} is spaced by $c/2 = 0.34$ nm, which matches the 0.32 nm spacing between the centers of the three COO$^-$ groups of citrate. In the $(\bar{1}010)_2$ plane, spacings of $c = 0.688$ nm match the distance between the terminal carboxylates of citrate. The structure shown is an idealization of the calcium- and hydroxide-deficient carbonated bone apatite; the actual surface is probably reconstructed (28) and significantly disordered. Adsorption of citrate purely at defects, such as steps on certain crystal faces, seems unlikely given its relatively high area density, and would result in stronger clustering of citrate, at the defects, than observed in CODEX NMR.

Citrate in bone is fundamentally different from carbonate, fluoride, sodium, magnesium, hydroxide (29), calcium, or phosphate ions, in that it is too large to be incorporated into the apatite crystal lattice. Therefore, bound citrate must remain an interfacial component that affects properties of the bone nanocomposite more profoundly than do simple substitutions of carbonate for phosphate or of sodium for calcium. Thus, we propose that citrate bound to the nanocrystal surface stabilizes the apatite nanocrystals by preventing their further growth. The crystallite thickness of 3 nm corresponds to only 4 unit cells, which results in a high surface energy that would make further crystal thickening favorable. Strongly bound citrate interferes with that thickening by inhibiting formation of additional phosphate layers. Indeed, it has been shown in vitro that hydroxyapatite forms thinner nanocrystals in the presence of citrate (30–32). In vivo, addition of citrate to calcium phosphate biocement for bone implants improves biocompatibility (32, 33), and various citrate nutritional supplements appear to prevent the onset of osteoporosis (34), presumably by stabilizing the apatite crystals.

Citrate also stabilizes hydroxyapatite relative to other calcium phosphates (35), possibly due to the good match between the spacing of the terminal COO$^-$ groups in citrate and the lattice parameter c in apatite. Furthermore, citrate bound to collagen, unlike neat collagen (7), initiates apatite crystallization in vitro (36). Thus, citrate might play an important role not only in stabilizing existing apatite nanocrystals, but also in crystal nucleation during biomineralization in bone. The importance of citrate in bone, which accounts for ~80% of all citrate in the body (14), is confirmed by its presence in a wide range of vertebrate classes, from fish to mammals, see Fig. 1 *A–C*. Citrate provides a larger number of carboxylates for calcium binding in bone than do the

proteins osteocalcin (37), osteopontin, and osteonectin (7) taken together.

Conclusions and Outlook

By means of advanced solid-state NMR spectroscopy and distance measurements, we have demonstrated that citrate is strongly bound to the apatite nanocrystals in bone. Citrate accounts for 5.5 wt% of the organic fraction of the nanocomposite in bone, and thus provides more COO^- groups for binding to calcium of apatite than all noncollagenous proteins in bone combined. The strong binding of citrate was proved by its close distance to apatite and absence of large-amplitude motions. After removing native citrate in bone by hot dilute acid treatment and replacing it with ^{13}C-labeled citrate, the distances of all carbons in citrate from the apatite surface were measured. Two of the three carboxylate carbons are slightly closer to the surface than are methylene and quaternary C, whose similar distances of ~0.4 nm show that the long axis of most citrate molecules is tilted only slightly relative to the surface. The spacing of COO^- groups in citrate matches that of calcium ions along the *c*-axis in apatite. The area density of citrate on bone apatite is around $1/(2\ \mathrm{nm})^2$, sufficient to make the nanocrystal surface less hydrophilic. On the basis of these data, a model of citrate bound to apatite was presented. Bound apatite clearly interferes with nanocrystal thickening and is found similarly in a wide range of vertebrate orders, which indicates its important role in stabilizing the size of the nanocrystals at the small thickness most favorable for mechanical properties and for fast resorption during bone remodeling.

The discovery of apatite-bound citrate in the bone nanocomposite leads to various intriguing research questions. What is the source of citrate in bone? At what stage of bone development does citrate appear? How is the abundance of citrate on the nanocrystal surface controlled? Is the citrate concentration abnormal in diseased bone? Further, the measured NMR distance data will be valuable as benchmarks for ab initio simulations of surface binding of functional molecules.

Methods

Compact (cortical) bone was obtained from the midsections of femur bone from a four-year-old cow and three-month-old chicken and cleaned of all muscular and connective tissue, and of the marrow. The poorly mineralized and porous surface layer of the femur was cut away with a sharp razor. Fish bone was obtained from the ribs of tilapia, a fresh-water fish, which was cooled to below 4 °C shortly after the animal had been killed. The bone was cryomilled in a *SPEX 6750 Freezer Mill* cryogenic grinder, washed in a 3:1 mixture of methanol and chloroform to remove any lipids, placed under vacuum at 0.01 Torr and 233 K to remove all traces of solvent, equilibrated at ambient humidity, and packed into 7-mm and 4-mm zirconia NMR rotors with Kel-F® caps.

^{13}C-labeled citrate-exchanged bovine bone was prepared with 1,5-$^{13}C_2$, 2,4-$^{13}C_2$, or $^{13}C_6$ citric acid, all obtained from Isotec. We made 2 mM citrate solutions by dissolving 5 mg of each ^{13}C-labeled citric acid in 13 mL deionized water, and adjusted the pH to 7.4 by using NaOH. In order to extract native citrate, degreased bovine bone powder was boiled at 80 °C for 24 h in dilute acid made from distilled water adjusted to pH = 4 using hydrochloric acid. The bone powder was removed from the dilute acid and washed until the supernatant was pH neutral, then incubated in the 2 mM citrate solution at 36.5 °C for 7 d under gentle shaking, in order to allow the ^{13}C-labeled citrate to diffuse into the bone. Next, the citrate-exchanged bovine bone was washed several times with deionized water to remove loosely attached citrate. The residual water was removed via lyophilization.

The ^{13}C-labeled citrate adsorbed onto the surface of NuOss™ bone mineral (deproteinized bovine bone, ACE Surgical Supply Co.) with particle size of 0.5–1.0 mm and specific surface area of 60 m^2/g was prepared as follows. We prepared 13 mL of 2 mM citrate solution by dissolving 5 mg citric-1,5-$^{13}C_2$ acid in 13 mL deionized water, and adjusted the pH to 7.4 using NaOH. After adding the bone mineral matrix into the citrate solution, the mixture was incubated at 36.5 °C with continuous gentle shaking overnight. The supernatant was decanted and the bone mineral was washed several times to remove loosely attached citrate. Residual water was removed by freeze-drying.

The NMR experiments were performed using a Bruker DSX-400 spectrometer at 100 MHz for ^{13}C, and 162 MHz for ^{31}P, in Bruker 7-mm double resonance (for spectroscopy and CODEX) and 4-mm triple resonance (for REDOR) magic-angle spinning probes at spinning frequencies between 4 and 6 kHz. The 90° pulse lengths were *ca.* 4.2 μs. Most of the ^{13}C spectra in Fig. 1 were recorded under magic-angle spinning of 5.3 kHz with total suppression of sidebands (38). The cross polarization contact time was 1 ms and the recycle delay 2.5 s. To select signals of carbons with weak C—H dipolar couplings, spectra were also acquired with additional 40 μs of gated decoupling before signal detection. ^{1}H-^{13}C wideline-separation spectra were measured on bovine bone at 4.3 kHz magic-angle spinning (MAS), with 0.2 ms standard Hartmann-Hahn cross polarization and 60 t_1-increments of 10 μs, using multiecho detection (39) with spectral resolution (40) for sensitivity enhancement and reduction of the measuring time by a factor of about 10.

^{13}C{^{31}P} REDOR (20) NMR data were obtained using a 4-mm Bruker triple resonance probehead at 6 kHz MAS with recoupling times of $Nt_r = 3$ ms, 4.66 ms, 6 ms, and 7.66 ms. A four-step phase cycle along with composite 90°-180°-90° ^{31}P recoupling pulses was used to minimize pulse length errors and achieve maximal dephasing (41). The ^{1}H composite-pulse decoupling power was $\gamma B_1/(2\pi) = 66$ kHz. Fig. 1*D* shows the sum of the ^{13}C{^{31}P} REDOR difference spectra $\Delta S = S_0$-S, where S_0 is the reference signal without pulses applied to ^{31}P. The total measuring time for the REDOR spectra of bone was 19 d. In uniformly ^{13}C-labeled citrate, ^{13}C-^{13}C J-couplings result in fast loss of the reference signal S_0 when the standard REDOR sequence is used. Therefore, the dephasing of C_q in uniformly ^{13}C-labeled citrate was measured by applying a selective soft Gaussian pulse of $\gamma B_1/(2\pi) = 1$ kHz, which removes the J-coupling effects (42), to the C_q resonance. CODEX ^{13}C NMR data were obtained for 1,5-$^{13}C_2$ citrate adsorbed onto the surface of NuOss™ bone mineral at 4-kHz MAS with mixing times up to 20 s, and multiecho detection was used for sensitivity enhancement.

ACKNOWLEDGMENTS. This work was supported by the Department of Energy, Office of Basic Energy Science, Division of Materials Sciences and Engineering, at the Ames Laboratory, under Contract No. DE-AC02-07CH11358.

1. Buckwalter JA, Glimcher MJ, Cooper RR, Recker R (1995) Bone biology .1. Structure, blood-supply, cells, matrix, and mineralization. *J Bone Joint Surg Am* 77A:1256–1275.
2. Currey JD (2002) *Bones* (Princeton University Press, Princeton, New Jersey) p 456.
3. Rey C, Combes C, Drouet C, Glimcher MJ (2009) Bone mineral: update on chemical composition and structure. *Osteoporos Int* 20:2155–2155.
4. Weiner S, Traub W (1992) Bone-structure—from Angstroms to microns. *FASEB J* 6:879–885.
5. Weiner S, Wagner HD (1998) The material bone: Structure mechanical function relations. *Annu Rev Mater Sci* 28:271–298.
6. Gao HJ, Ji BH, Jager IL, Arzt E, Fratzl P (2003) Materials become insensitive to flaws at nanoscale: lessons from nature. *Proc Natl Acad Sci USA* 100:5597–5600.
7. Zhu W, Robey PG, Boskey AL (2008) The regulatory role of matrix proteins in mineralization of bone. *Osteoporosis*, eds R Markus, D Feldman, DA Nelson, and CJ Rosen (Elsevier Academic Press, San Diego, CA), Vol 1.
8. Hartgerink JD, Beniash E, Stupp SI (2001) Self-assembly and mineralization of peptide-amphiphile nanofibers. *Science* 294:1684–1688.
9. Hu YY, et al. (2009) Self-assembled calcium phosphate nanocomposites using block copolypeptide templates. *Soft Matter* 5:4311–4320.
10. Johnsson M, Richardson CF, Bergey EJ, Levine MJ, Nancollas GH (1991) The effects of human salivary cystatins and statherin on hydroxyapatite crystallization. *Archs Oral Biol* 36:631–636.
11. Hunter GK, Kyle LC, Goldberg HA (1994) Modulation of crystal formation by bone phosphoproteins: structural specificity of the osteopontin-mediated inhibition of hydroxyapatite formation. *Biochem J* 300:723–728.
12. Spoerke ED, Anthony SG, Stupp SI (2009) Enzyme directed templating of artifical bone mineral. *Adv Mater* 21:425–430.
13. Dickens F (1941) The citric acid content of animal tissues, with reference to its occurrence in bone and tumor. *Biochem J* 35:1011–1023.
14. Hartles RL (1964) Citrate in mineralized tissues. *Advances in Oral Biology* 1:225–253.
15. Currey JD (2003) Role of collagen and other organics in the mechanical properties of bone. *Osteoporos Int* 14:S29–S36.
16. Posner AS, Beebe RA (1975) Surface chemistry of bone mineral and related calcium phosphates. *Semin Arthritis Rheu* 4:267–291.
17. Jaeger C, et al. (2005) Investigation of the nature of the protein-mineral interface in bone by solid-state NMR. *Chem Mat* 17:3059–3061.
18. Wise ER, et al. (2007) The organic-mineral interface in bone is predominantly polysaccharide. *Chem Mater* 19:5055–5057.
19. Zhu PZ, et al. (2009) Time-resolved dehydration-induced structural changes in an intact bovine cortical bone revealed by solid-state NMR spectroscopy. *J Am Chem Soc* 131:17064–17065.
20. Gullion T, Schaefer J (1989) Detection of weak heteronuclear couplings by REDOR. *Adv Magn Reson* 13:57–83.

21. Ndao M, et al. (2009) A $^{13}C(^{31}P)$ REDOR NMR investigation of the role of glutamic acid residues in statherin-hydroxyapatite recognition. *Langmuir* 25:12136–12143.
22. Schmidt-Rohr K, Clauss J, Spiess HW (1992) Correlation of structure, mobility, and morphological information in heterogeneous polymer materials by two-dimensional wideline-separation NMR spectroscopy. *Macromolecules* 25:3273–3277.
23. Best SM, Duer MJ, Reid DG, Wise ER, Zou S (2008) Towards a model of the mineral-organic interface in bone: NMR of the structure of synthetic glycosaminoglycan- and polyaspartate-calcium phosphate composites. *Mag Reson Chem* 46:323–329.
24. de Leeuw NH, Rabone JAL (2007) Molecular dynamics simulations of the interaction of citric acid with the hydroxyapatite (0001) and (01$\bar{1}$0) surfaces in an aqueous environment. *Crystengcomm* 9:1178–1186.
25. Misra DN (1996) Interaction of citric acid with hydroxyapatite: surface exchange of ions and precipitation of calcium citrate. *J Dent Res* 75:1418–1425.
26. deAzevedo ER, Hu W-G, Bonagamba TJ, Schmidt-Rohr K (1999) Centerband-only detection of exchange: efficient analysis of dynamics in solids by NMR. *J Am Chem Soc* 121:8411–8412.
27. Terpstra RA, et al. (1986) F-faces of apatite and its morphology—theory and observation. *J Cryst Growth* 78:468–478.
28. Mathew M, Takagi S (2001) Structures of biological minerals in dental research. *Journal of Research of the National Institute of Standards and Technology* 106:1035–1044.
29. Cho G, Wu Y, Ackerman JL (2003) Detection of hydroxyl ions in bone mineral by solid-state NMR spectroscopy. *Science* 300:1123–1127.
30. Tenhuisen KS, Brown PW (1994) The effects of citric and acetic acids on the formation of calcium-deficient hydroxyapatite at 38 °C. *J Mater Sci: Mater M* 5:291–298.
31. Lopez-Macipe A, Gomez-Morales J, Rodriguez-Clemente R (1998) Nanosized hydroxyapatite precipitation from homogeneous calcium/citrate/phosphate solutions using microwave and conventional heating. *Adv Mater* 10:49–53.
32. Hempel U, Reinstorf A, Poppe W, Wenzel KW (2004) Proliferation and differentiation of osteoblastson Biocement D modified with collagen type I and citric acid. *J Biomed Mater Res B* 71:130–143.
33. Schneiders W, et al. (2007) Effect of modification of hydroxyapatite/collagen composites with sodium citrate, phosphoserine, phosphoserine/RGD-peptide and calcium carbonate on bone remodelling. *Bone* 40:1048–1059.
34. Karp HJ, Ketola ME, Lamberg-Allardt CJE (2009) Acute effects of calcium carbonate, calcium citrate, and potassium citrate on markers of calcium and bone metabolism in young women. *Brit J Nutr* 102:1341–1347.
35. Jiang WG, et al. (2009) Biomimetically triggered inorganic crystal transformation by biomolecules: a new understanding of biomineralization. *J Phys Chem B* 113:10838–10844.
36. Rhee SH, Tanaka J (1999) Effect of citric acid on the nucleation of hydroxyapatite in a simulated body fluid. *Biomaterials* 20:2155–2160.
37. Hoang QQ, Sicheri F, Howard AJ, Yang DSC (2003) Bone recognition mechanism of porcine osteocalcin from crystal structure. *Nature* 425:977–980.
38. Dixon WT (1982) Spinning-sideband-free and spinning-sideband-only NMR spectra of spinning samples. *J Chem Phys* 77:1800–1809.
39. Hou SS, Beyer FL, Schmidt-Rohr K (2002) High-sensitivity multinuclear NMR spectroscopy of a smectite clay and of clay-intercalated polymer. *Solid State Nucl Mag* 22:110–127.
40. Trebosc J, Wiench JW, Huh S, Lin VSY, Pruski M (2005) Studies of organically functionalized mesoporous silicas using heteronuclear solid state correllation NMR spectroscopy under fast magic-angle-spinning. *J Am Chem Soc* 127:7587–7593.
41. Sinha N, Schmidt-Rohr K, Hong M (2004) Compensation of pulse imperfections in rotational-echo double resonance NMR by composite pulses and EXORCYCLE. *J Magn Reson* 168:358–365.
42. Jaroniec CP, Tounge BA, Rienstra CM, Herzfeld J, Griffin RG (1999) Measurement of ^{13}C-^{15}N distances in uniformly ^{13}C labeled biomolecules: J-decoupled REDOR. *J Am Chem Soc* 121:10237–10238.